A neuroendocrine principle: Pancreatic islets actively shape sympathetic innervation

Authors:

Dong-Xue Li[1,†], Jia-Mei Luo[1,†], Jun-Jie Wang[1,†], Yun-Zhen Qian[1,†], Dilinazi Abudujilile[1,†], Musitaba Mutailifu[1], Tian Yang[1], Yuan-Xin Hong[1], Wen-Tao Shi[1], Xiao-Yi Ma[1], Qing Ye[1], Lei Zhu[1], Hui-Li[1], Xiao-Mei Yang[1], Yan-Li Zhang[1], Shu-Heng Jiang[1], Yan-Qiu Yu[2], Kai Wang[3], Jun Li[1], Qing Li[1], Li-Peng Hu[1,*], Xue-Li Zhang[1,*], Zhi-Gang Zhang[1,*]

Affiliations:

[1] State Key Laboratory of Systems Medicine for Cancer, Shanghai Cancer Institute, Ren Ji Hospital, School of Medicine, Shanghai Jiao Tong University, Shanghai, China.

[2] Department of Pathophysiology, Basic Medical College, China Medical University, Shenyang, China

[3] Department of Physiology and Pathophysiology, School of Basic Medical Sciences, Peking University, Beijing, China

[†]Dong-Xue Li, Jia-Mei Luo, Jun-Jie Wang, Yun-Zhen Qian and Dilinazi Abudujilile contributed equally to this work.

*Corresponding authors: Zhi-Gang Zhang, E-mail: zzhang@shsci.org; or Xue-Li Zhang, E-mail: xlzhang@shsci.org; or Li-Peng Hu, E-mail: lphu@shsci.org

Abstract

Survival critically depends on maintaining blood glucose levels to provide essential energy, especially during emergencies such as the fight-or-flight response, when timely glucose control via neural integration is vital. However, pancreatic islets constitute only a small fraction of the pancreas and are dispersed throughout the organ, raising the fundamental question of how the nervous system coordinates synchronized control of multiple islets. Using whole-organ clearing and 3D imaging, we mapped pancreatic sympathetic innervation, revealing specialized anatomical integration between sympathetic nerves and islets. Transplanted islets intrinsically attracted sympathetic nerves independent of their native environment. Chronic islet injury disrupted sympathetic innervation and markedly impaired nerve regeneration after denervation. Sympathetic denervation markedly elevated islet-derived Reg2 and Reg3β; administration of these proteins accelerated sympathetic regeneration and improved islet graft function. Our findings identify an islet-sympathetic architecture actively maintained by islets, uncovering an endocrine-driven mechanism for neural regulation, highlighting Reg2 and Reg3β as therapeutic candidates for diabetes management.

Introduction

Precise coordination between the nervous and endocrine systems is essential for maintaining metabolic homeostasis and enabling rapid physiological adaptation[1–6]. Pancreatic islets, highly specialized endocrine micro-organs that tightly regulate blood glucose levels, depend heavily on neural inputs to rapidly and dynamically adjust hormone secretion in response to fluctuating metabolic demands[7–14]. In particular, during acute metabolic emergencies such as hypoglycemia or the fight-or-flight response, timely and synchronized regulation of pancreatic islets by the sympathetic nervous system is crucial for restoring blood glucose levels and thus ensuring survival. However, given their dispersed distribution within the pancreas, how sympathetic nerves coordinate rapid and synchronized control of multiple islets under these critical conditions remains unclear. This suggests a specialized neural-islet architecture supporting such coordinated control — an anatomical relationship conventional two-dimensional histological methods cannot resolve at the whole-organ scale[15–20].

Recently, advances in whole-organ tissue clearing combined with 3D imaging have opened new possibilities to address these critical technical challenges, enabling investigations into islet microstructure, vascular networks, and neural innervation at unprecedented spatial resolution[21–27]. Nevertheless, due to the inherently soft, anatomically complex, and highly convoluted nature of mouse pancreatic tissue, precisely mapping the global 3D structural relationships between islets and neural networks remains technically challenging. Here, we overcame these technical

limitations by fully unfolding the pancreas and employing whole-organ tissue clearing combined with advanced 3D imaging. This enabled us to identify an intimate structural association specifically between sympathetic nerves and pancreatic islets, a relationship notably absent for parasympathetic and sensory nerves.

Building on this newly identified anatomical relationship, we further explored its underlying mechanisms. Developmental studies have previously demonstrated that disruption of sympathetic innervation during early pancreatic development severely impairs islet architecture and profoundly compromises hormone secretion[28,29], reinforcing the classical view of islets as passive recipients of neural inputs whose structural and functional integrity critically depends on innervation. Extending this classical view, our findings provide evidence that the intimate structural relationship between sympathetic nerves and pancreatic islets is actively established and maintained by the islets themselves. These results significantly expand our understanding of endocrine-neural interactions, highlighting an active role for islets in shaping their neural environment.

Results

1. Pancreatic islets are intimately and regularly associated with sympathetic nerves

We first performed a robust method to fully unfold the convoluted mouse pancreas (Extended Data Fig.1a), enabling efficient whole-pancreas tissue clearing (Extended Data Fig.1b). Subsequent advanced 3D imaging provided unprecedented visualization of pancreatic neural networks and their precise spatial relationships with pancreatic islets. To comprehensively characterize the innervation pattern, we specifically labeled sympathetic nerves with tyrosine hydroxylase (TH), parasympathetic nerves with vesicular acetylcholine transporter (VAChT), and sensory nerves with calcitonin gene-related peptide (CGRP). These nerves were labeled in magenta fluorescence, while islets were labeled with insulin (green) and nuclei with DAPI (blue).

Strikingly, sympathetic nerves exhibited a highly organized architecture analogous to "electrical wiring", characterized by a prominent central conduit traversing the pancreas and numerous finer branches extensively distributed throughout the tissue (Fig.1a; Supplementary Video 1). Pancreatic islets were not randomly scattered but precisely positioned along these sympathetic nerve fibers, reminiscent of "light bulbs" systematically arranged along "electrical cords" (Fig.1a-d). High-resolution imaging confirmed intimate spatial contacts between sympathetic fibers and pancreatic islets (Fig.1e), clearly illustrated by 3D reconstructions (Fig.1f, g). This anatomical organization might function similarly to "electrical wiring" powering synchronized

illumination of connected “bulbs”, enabling islets to simultaneously respond to sympathetic signals. We also examined parasympathetic and sensory innervation in relation to pancreatic islets but did not observe the structured, “wiring-light bulb”-like arrangement seen with sympathetic nerves (Extended Data Fig.2; Supplementary Videos 2, 3).

The unique anatomical arrangement between islets and sympathetic nerves likely supports their coordinated biological functions. However, it remains unclear how this pattern arises — whether determined by the pancreatic environment or actively shaped by islets themselves.

2. Islets recruit sympathetic nerves independently of the pancreatic environment

To distinguish between these two possibilities, we isolated approximately 500 islets from healthy 8-week-old mice and transplanted them beneath the renal capsule of streptozotocin (STZ)-induced diabetic mice[30,31], establishing a heterotopic transplantation model (Fig.2a). Using this system, we rigorously tested whether islets could intrinsically establish similar spatial relationships with sympathetic nerves independent of their native pancreatic environment. Post-transplantation monitoring confirmed graft viability and restored endocrine function, indicated by normalized blood glucose levels (Extended Data Fig.3b, e). Notably, the model employed here was primarily intended to investigate biological mechanisms rather than to serve as a therapeutic approach for diabetes.

We performed whole-kidney 3D imaging at day 120 post-transplantation, which clearly demonstrated sympathetic innervation of transplanted islets (islets, green; sympathetic nerves, magenta) from both horizontal (0°) and tilted (45°) perspectives (Fig.2b; Supplementary Video 4). At day 120, sympathetic fibers were notably extended toward the transplanted islets. (Fig.2b, left; white arrowheads). To capture the dynamics of sympathetic nerve recruitment, we conducted tissue clearing imaging at intermediate time points (days 10, 20, 30, 40, and 50; Extended Data Fig.3a left; Supplementary Videos 5-9). Directional nerve growth toward transplanted islets was evident as early as day 10 and progressively strengthened. Quantitative analysis (Extended Data Fig.3c, d) revealed a significant increase in sympathetic nerve growth and branching at day 50 compared to day 10.

We performed detailed 3D reconstruction to clearly distinguish newly extended, islet-recruited sympathetic nerves (yellow, indicated by white arrowheads) from pre-existing renal sympathetic nerves (magenta), along with transplanted islets (green) and the adrenal gland (blue) (Fig. 2b, right; Extended Data Fig.3a, right; Supplementary Videos 4-9). Quantitative analysis revealed a progressive increase in sympathetic nerve length and branching toward transplanted islets, reaching significantly elevated levels by 120 days post-transplantation (Fig.2c, d).

3. Islets maintain sympathetic innervation and promote regeneration after denervation

Based on our finding that transplanted islets actively recruit sympathetic nerves in an ectopic environment, we next explored whether islets similarly regulate sympathetic innervation within their native pancreatic environment.

Initially, during experiments involving chronic islet injury induced by STZ, we unexpectedly observed pronounced disruption of pancreatic sympathetic nerves approximately 140 days post-treatment (Fig.3a, right; Supplementary Video 10). In contrast, control mice receiving solvent injections maintained sympathetic nerve architecture (Fig.3a, left; Supplementary Video 11). This finding revealed a previously unrecognized role of islets in maintaining pancreatic sympathetic nerve integrity.

Subsequently, to determine whether islets exhibit similar nerve-attracting properties within the native pancreas, we selectively ablated sympathetic nerves via intrapancreatic injection of 6-hydroxydopamine (6-OHDA). Successful denervation was confirmed at early time points (Extended Data Fig.4; Supplementary Videos 12-14). As anticipated, time-course analyses (days 47, 56, and 65 post-denervation) revealed progressive regeneration of sympathetic nerves and re-established organized interactions with islets (Fig.3b, upper; Supplementary Videos 15-17). By contrast, severe islet injury induced by STZ administration one day post-denervation markedly impaired nerve regeneration, resulting in sparse, disorganized sympathetic fibers (Fig.3b, lower; Supplementary Videos 18-20). Control mice injected with solvents

171 maintained sympathetic innervation, ruling out nonspecific effects of vehicle injections.
172 (Extended Data Fig.5; Supplementary Videos 21-23).
173
174 These results collectively revealed an essential and previously unrecognized role of
175 pancreatic islets in maintaining sympathetic nerve integrity under physiological
176 conditions and actively promoting nerve regeneration following injury, likely through
177 the secretion of specific molecular factors.
178
179 **4. Sympathetic denervation induces islet-specific upregulation of Reg-family**
180 **proteins, especially Reg2 and Reg3β**
181 To investigate the molecular mechanisms underlying islet-induced sympathetic nerve
182 regeneration, we utilized the in situ sympathetic nerve ablation model induced by 6-
183 OHDA described above. On day 7 post-denervation, pancreatic islets were directly
184 isolated from their native pancreatic environment by laser-capture microdissection
185 (LCM) (Fig.4a). This approach preserved the native state of the islets and avoided
186 potential alterations in their secretory profiles during isolation. Subsequent mRNA
187 sequencing analysis revealed significant changes in gene expression, particularly a
188 marked upregulation of regenerating gene family (Reg-family) members, notably *Reg2*
189 and *Reg3b* (Fig. 4b).
190
191 To further clarify the dynamic expression patterns of Reg-family genes following
192 sympathetic nerve injury, and to obtain sufficient islet samples for analysis at multiple

193 time points, we subsequently utilized conventional islet isolation methods to collect
194 islets at days 3, 7, 14, and 21 post-denervation for additional mRNA sequencing
195 analysis (Fig.4c). Consistent with the LCM-based findings, most Reg-family members,
196 particularly *Reg2 and Reg3b*, exhibited significantly elevated expression levels from
197 day 7 onward (Fig.4d). These findings were independently validated by real-time
198 quantitative PCR (RT-qPCR) analysis, confirming significant upregulation of *Reg2 and*
199 *Reg3b* (Fig.4e). Given that Reg-family proteins are well-established secretory factors
200 implicated in tissue repair and regeneration[32–34], our results strongly suggest that islet-
201 derived Reg-family proteins, particularly Reg2 and Reg3β, serve as key molecular cues
202 guiding sympathetic nerve regeneration toward pancreatic islets.
203

204 **5. Exogenous Reg2 and Reg3β accelerate sympathetic nerve growth and enhance**
205 **islet graft function**

206 To functionally validate the importance of Reg2 and Reg3β and explore potential
207 translational implications, we initially transplanted pancreatic islets encapsulated in a
208 hydrogel matrix containing exogenous recombinant Reg2 (rReg2) and Reg3β (rReg3β)
209 beneath the renal capsule of recipient mice. At day 50 post-transplantation, whole-
210 kidney clearing and 3D imaging revealed that local administration of rReg2 and rReg3β
211 significantly enhanced sympathetic nerve regeneration, as evidenced by increased
212 nerve length, branching, and directional growth toward transplanted islets compared
213 with controls (Fig.5a, b; Supplementary Video 24).
214

215 Given the potential limitations of local protein delivery in clinical contexts, we next
216 evaluated whether systemic administration of rReg2 and rReg3β could similarly

217 enhance sympathetic regeneration. Recombinant proteins were administered
218 intraperitoneally (i.p.) on days 1, 3, and 5 post-transplantation. Tissues analyzed 35
219 days post-transplantation showed that systemic delivery also robustly promoted
220 sympathetic regeneration, with significantly increased nerve length and branching
221 toward transplanted islets (Fig.5c, d; Supplementary Video 25).
222
223 To further confirm that endogenous Reg2 and Reg3β specifically mediate sympathetic
224 nerve regeneration toward islets, we used lentiviral-mediated RNA interference to
225 knock down *Reg2* and *Reg3b* expression in isolated islets prior to transplantation
226 (lentiviral sequences provided in Supplementary Table 1), and knockdown efficiency
227 was confirmed by RT-qPCR analysis (Extended Data Fig.6d). At day 60 post-
228 transplantation, sympathetic regeneration toward islets with *Reg2* and *Reg3b*
229 knockdown was significantly delayed, characterized by reduced nerve length and
230 branching compared to controls (Fig.5e, f; Supplementary Video 26).
231
232 Representative whole-kidney clearing images and corresponding 3D reconstructions
233 (horizontal 0° view, Fig.5a, c, e; titled 45° view, Extended Data Fig.6a-c)
234 comprehensively illustrate the spatial interactions between sympathetic nerves and
235 transplanted islets under these experimental conditions. White arrowheads indicate
236 sympathetic fibers clearly directed toward the transplanted islets.
237
238 To evaluate whether Reg2 and Reg3β-mediated sympathetic nerve regeneration
239 functionally enhances transplanted islets, we administered combined local and systemic
240 rReg2 and rReg3β treatment during islet transplantation. Subsequently, intraperitoneal
241 glucose tolerance tests (IPGTT) were performed at days 30 and 50 post-transplantation.

Mice receiving rReg2 and rReg3β-treated islets exhibited significantly improved glucose tolerance compared to controls receiving islets alone. Notably, this functional enhancement was more pronounced at day 50 than at day 30 (Fig.5g, h). These results suggest that Reg2 and Reg3β not only accelerate but also support prolonged functional performance of transplanted islets, highlighting the therapeutic promise of Reg proteins for enhancing clinical outcomes in islet transplantation and managing diabetes more effectively (Supplementary Video 27).

Discussion

Pancreatic islets, essential regulators of glucose homeostasis, are dispersed micro-organs within the pancreas[35,36]. This unique distribution enables islets to precisely monitor and rapidly respond to glucose fluctuations, yet raises a fundamental physiological question: how do dispersed islets achieve synchronized neural integration during acute metabolic stress, such as severe hypoglycemia or fight-or-flight responses[37–39]? Here, we reveal for the first time a precise, "wiring-light bulb" anatomical arrangement, where islets ("light bulbs") align closely along fine sympathetic nerve branches ("wiring"). This specialized organization provides a structural foundation for rapid and coordinated neural integration, analogous to multiple bulbs simultaneously illuminating once electrical current passes through the wiring, highlighting how "**structure dictates function"** in neural signaling.

Using renal subcapsular transplantation, we confirmed that pancreatic islets actively shape their specialized sympathetic innervation independently of the pancreatic

environment, and similarly promote sympathetic nerve regeneration following injury within the native pancreas. Notably, chronic islet injury resulted in progressive disruption of pancreatic sympathetic networks, further uncovering a previously unrecognized role of islets in actively maintaining sympathetic neural integrity. These findings collectively challenge the classical view of endocrine organs as passive neural targets[40,41], revealing instead their active participation in both establishing and preserving neural architecture. This introduces a novel biological paradigm for organ-nerve interactions: **function shapes and sustains structure**, a principle potentially applicable to other endocrine organs.

Here, we identified Reg-family proteins, particularly Reg2 and Reg3β, as critical mediators enhancing both islet graft function and sympathetic nerve regeneration, with therapeutic efficacy notably increasing over time. Traditionally associated with inflammation[42,43], tissue repair[44], and regeneration[34,45], Reg proteins had not previously been studied in a neuro-endocrine context. Our findings substantially expand the functional repertoire of these proteins, uncovering their novel capacity to directly facilitate sympathetic nerve growth and promote the functional maturation of transplanted islets. This dual role positions Reg2 and Reg3β as promising therapeutic candidates not only for improving clinical outcomes in islet transplantation but also for preserving sympathetic nerve integrity compromised during diabetes progression. Further exploration of their translational potential could provide innovative strategies for managing metabolic and neural complications associated with diabetes.

Despite these advances, key questions remain unanswered. First, it remains unclear whether the specialized anatomical arrangement between sympathetic nerves and pancreatic islets observed in mice is conserved in humans. Second, although we identified Reg2 and Reg3β as critical mediators of sympathetic nerve regeneration, their specific cellular sources, molecular mechanisms, and signaling pathways within islets require further elucidation. Future studies using human islets or organoids combined with single-cell RNA sequencing and spatial transcriptomics could address these gaps. Finally, optimal delivery methods, precise dosage, and combinations with other neurotrophic factors must be defined to facilitate clinical translation.

In summary, our findings redefine the fundamental relationship between endocrine organs and neural networks, uncovering a previously unrecognized biological principle whereby pancreatic islets actively construct and sustain their specialized sympathetic architecture. This reveals an innovative paradigm in neuro-endocrine biology: endocrine function is not passively regulated by neural inputs but rather actively shapes and maintains neural circuits to optimize physiological outcomes. By identifying Reg2 and Reg3β as critical molecular orchestrators, we open avenues for novel therapeutic strategies not only for diabetes but potentially for broader metabolic and neurological disorders where neural integrity is compromised. Future research should explore whether similar organ-driven neural remodeling occurs across other endocrine systems, providing generalizable insights into organ-nerve interactions and expanding therapeutic possibilities for metabolic and neurological disorders.

References: Manuscripts

1. Thorens, B. (2010). Central control of glucose homeostasis: the brain – endocrine pancreas axis. Diabetes. Metab. *36*, S45–S49. https://doi.org/10.1016/S1262-3636(10)70466-3.

2. Faber, C.L., Deem, J.D., Campos, C.A., Taborsky, G.J., and Morton, G.J. (2020). CNS control of the endocrine pancreas. Diabetologia *63*, 2086–2094. https://doi.org/10.1007/s00125-020-05204-6.

3. Hyun, U., and Sohn, J.-W. (2022). Autonomic control of energy balance and glucose homeostasis. Exp. Mol. Med. *54*, 370–376. https://doi.org/10.1038/s12276-021-00705-9.

4. Jimenez-Gonzalez, M., Li, R., Pomeranz, L.E., Alvarsson, A., Marongiu, R., Hampton, R.F., Kaplitt, M.G., Vasavada, R.C., Schwartz, G.J., and Stanley, S.A. (2022). Mapping and targeted viral activation of pancreatic nerves in mice reveal their roles in the regulation of glucose metabolism. Nat. Biomed. Eng. *6*, 1298–1316. https://doi.org/10.1038/s41551-022-00909-y.

5. Martinez-Sanchez, N., Sweeney, O., Sidarta-Oliveira, D., Caron, A., Stanley, S.A., and Domingos, A.I. (2022). The sympathetic nervous system in the 21st century: Neuroimmune interactions in metabolic homeostasis and obesity. Neuron *110*, 3597–3626. https://doi.org/10.1016/j.neuron.2022.10.017.

6. Agerskov, R.H., and Nyeng, P. (2024). Innervation of the pancreas in development

and disease. Development *151*, dev202254. https://doi.org/10.1242/dev.202254.

7. Ahrén, B., Ericson, L.E., Lundquist, I., Lorén, I., and Sundler, F. (1981). Adrenergic innervation of pancreatic islets and modulation of insulin secretion by the sympatho-adrenal system. Cell. Tissue. Res. *216*, 15–30. https://doi.org/10.1007/BF00234541.

8. Ahrén, B. (2000). Autonomic regulation of islet hormone secretion – Implications for health and disease. Diabetologia *43*, 393–410. https://doi.org/10.1007/s001250051322.

9. Rodriguez-Diaz, R., Speier, S., Molano, R.D., Formoso, A., Gans, I., Abdulreda, M.H., Cabrera, O., Molina, J., Fachado, A., Ricordi, C., et al. (2012). Noninvasive in vivo model demonstrating the effects of autonomic innervation on pancreatic islet function. Proc. Natl. Acad. Sci. U.S.A. *109*, 21456–21461. https://doi.org/10.1073/pnas.1211659110.

10. Rodriguez-Diaz, R., and Caicedo, A. (2014). Neural control of the endocrine pancreas. Best Pract. Res. Clin. Endocrinol. Metab. *28*, 745–756. https://doi.org/10.1016/j.beem.2014.05.002.

11. Proshchina, A.E., Krivova, Y.S., Barabanov, V.M., and Saveliev, S.V. (2014). Ontogeny of neuro-insular complexes and islets innervation in the human pancreas. Front. Endocrinol. (Lausanne) *5*, 57. https://doi.org/10.3389/fendo.2014.00057.

12. Li, W., Yu, G., Liu, Y., and Sha, L. (2019). Intrapancreatic Ganglia and Neural

Regulation of Pancreatic Endocrine Secretion. Front. Neurosci. *13*. https://doi.org/10.3389/fnins.2019.00021.

13. Lin, E.E., Scott-Solomon, E., and Kuruvilla, R. (2021). Peripheral Innervation in the Regulation of Glucose Homeostasis. Trends. Neurosci. *44*, 189–202. https://doi.org/10.1016/j.tins.2020.10.015.

14. Papazoglou, I., Lee, J.-H., Cui, Z., Li, C., Fulgenzi, G., Bahn, Y.J., Staniszewska-Goraczniak, H.M., Piñol, R.A., Hogue, I.B., Enquist, L.W., et al. (2022). A distinct hypothalamus-to-β-cell circuit modulates insulin secretion. Cell Metab. *34*, 285-298.e7. https://doi.org/10.1016/j.cmet.2021.12.020.

15. Cabrera-Vásquez, S., Navarro-Tableros, V., Sánchez-Soto, C., Gutiérrez-Ospina, G., and Hiriart, M. (2009). Remodelling sympathetic innervation in rat pancreatic islets ontogeny. BMC. Dev. Biol. *9*, 34. https://doi.org/10.1186/1471-213X-9-34.

16. Rodriguez-Diaz, R., and Caicedo, A. (2013). Novel approaches to study the role innervation plays in the biology of pancreatic islets. Endocrinol. Metab. Clin. North Am. *42*, 39–56. https://doi.org/10.1016/j.ecl.2012.11.001.

17. Campbell-Thompson, M., Butterworth, E.A., Boatwright, J.L., Nair, M.A., Nasif, L.H., Nasif, K., Revell, A.Y., Riva, A., Mathews, C.E., Gerling, I.C., et al. (2021). Islet sympathetic innervation and islet neuropathology in patients with type 1 diabetes. Sci. Rep. *11*, 6562. https://doi.org/10.1038/s41598-021-85659-8.

18. Lkhagvasuren, B., Mee-inta, O., Zhao, Z.-W., Hiramoto, T., Boldbaatar, D., and

Kuo, Y.-M. (2021). Pancreas-Brain Crosstalk. Front. Neuroanat. *15*, 691777. https://doi.org/10.3389/fnana.2021.691777.

19. Makhmutova, M., and Caicedo, A. (2021). Optical Imaging of Pancreatic Innervation. Front. Endocrinol. (Lausanne) *12*, 663022. https://doi.org/10.3389/fendo.2021.663022.

20. Krivova, Y.S., Proshchina, A.E., Otlyga, D.A., Leonova, O.G., and Saveliev, S.V. (2022). Prenatal development of sympathetic innervation of the human pancreas. Ann. Anat.-Anat. Anz *240*, 151880. https://doi.org/10.1016/j.aanat.2021.151880.

21. Tseng, S.-J., Lee, Y.-H., Chen, Z.-H., Lin, H.-H., Lin, C.-Y., and Tang, S.-C. (2009). Integration of optical clearing and optical sectioning microscopy for three-dimensional imaging of natural biomaterial scaffolds in thin sections. J. Biomed. Opt. *14*, 044004. https://doi.org/10.1117/1.3158998.

22. Fu, Y.-Y., Lu, C.-H., Lin, C.-W., Juang, J.-H., Enikolopov, G., Sibley, E., Chiang, A.-S., and Tang, S.-C. (2010). Three-dimensional optical method for integrated visualization of mouse islet microstructure and vascular network with subcellular-level resolution. J. Biomed. Opt. *15*, 046018. https://doi.org/10.1117/1.3470241.

23. Chiu, Y.-C., Hua, T.-E., Fu, Y.-Y., Pasricha, P.J., and Tang, S.-C. (2012). 3-D imaging and illustration of the perfusive mouse islet sympathetic innervation and its remodelling in injury. Diabetologia *55*, 3252–3261. https://doi.org/10.1007/s00125-012-2699-6.

24. Tang, S.-C., Peng, S.-J., and Chien, H.-J. (2014). Imaging of the islet neural network. Diabetes. Obes. Metab. *16*, 77–86. https://doi.org/10.1111/dom.12342.

25. Yang, Y.H.C., Kawakami, K., and Stainier, D.Y. (2018). A new mode of pancreatic islet innervation revealed by live imaging in zebrafish. eLife *7*, e34519. https://doi.org/10.7554/eLife.34519.

26. Alvarsson, A., Jimenez-Gonzalez, M., Li, R., Rosselot, C., Tzavaras, N., Wu, Z., Stewart, A.F., Garcia-Ocaña, A., and Stanley, S.A. (2020). A 3D atlas of the dynamic and regional variation of pancreatic innervation in diabetes. Sci. Adv. *6*, eaaz9124. https://doi.org/10.1126/sciadv.aaz9124.

27. Alvarsson, A., Jimenez-Gonzalez, M., Li, R., Rosselot, C., Tzavaras, N., Wu, Z., and Stanley, S.A. (2021). Optical Clearing and 3D Analysis Optimized for Mouse and Human Pancreata. Bio-protocol *11*, e4103. https://doi.org/10.21769/BioProtoc.4103.

28. Borden, P., Houtz, J., Leach, S.D., and Kuruvilla, R. (2013). Sympathetic Innervation during Development Is Necessary for Pancreatic Islet Architecture and Functional Maturation. Cell Rep. *4*, 287–301. https://doi.org/10.1016/j.celrep.2013.06.019.

29. Scott-Solomon, E., Boehm, E., and Kuruvilla, R. (2021). The sympathetic nervous system in development and disease. Nat. Rev. Neurosci. *22*, 685–702. https://doi.org/10.1038/s41583-021-00523-y.

30. Szot, G.L., Koudria, P., and Bluestone, J.A. (2007). Transplantation of Pancreatic Islets Into the Kidney Capsule of Diabetic Mice. J. Vis. Exp. *9*, 404. https://doi.org/10.3791/404.

31. Li, D., Kong, W., Hong, Y., Zhang, W., Sun, B., Wang, X., and Wang, K. (2025). Protocol for isolation and transplantation of rat pancreatic islets in the kidney capsule to treat diabetes. Star. Protoc. *6*, 103486. https://doi.org/10.1016/j.xpro.2024.103486.

32. Okamoto, H. (1999). The Reg gene family and Reg proteins: with special attention to the regeneration of pancreatic beta-cells. J. Hepatobiliary. Pancreat. Surg. *6*, 254–262. https://doi.org/10.1007/s005340050115.

33. Wu, H., Zheng, Q., Rengabhashyam, P., and Zenilman, M.E. (2000). A Brief History of Pancreatic Reg: Implications as to its Clinical Importance. Einstein Q. J. Biol. Med. *17*, 178.

34. Namikawa, K., Fukushima, M., Murakami, K., Suzuki, A., Takasawa, S., Okamoto, H., and Kiyama, H. (2005). Expression of Reg/PAP family members during motor nerve regeneration in rat. Biochem. Biophys. Res. Commun. *332*, 126–134. https://doi.org/10.1016/j.bbrc.2005.04.105.

35. Röder, P.V., Wu, B., Liu, Y., and Han, W. (2016). Pancreatic regulation of glucose homeostasis. Exp. Mol. Med. *48*, e219. https://doi.org/10.1038/emm.2016.6.

36. Abdulreda, M.H., and Berggren, P.O. (2021). The pancreatic islet: a micro-organ in

429 control. CellR4 *9*, e3093. https://doi.org/10.32113/cellr4_20213_3093.

430 37. Morton, G.J., Muta, K., Kaiyala, K.J., Rojas, J.M., Scarlett, J.M., Matsen, M.E.,
431 Nelson, J.T., Acharya, N.K., Piccinini, F., Stefanovski, D., et al. (2017). Evidence
432 That the Sympathetic Nervous System Elicits Rapid, Coordinated, and Reciprocal
433 Adjustments of Insulin Secretion and Insulin Sensitivity During Cold Exposure.
434 Diabetes *66*, 823–834. https://doi.org/10.2337/db16-1351.

435 38. Noguchi, G.M., and Huising, M.O. (2019). Integrating the inputs that shape
436 pancreatic islet hormone release. Nat. Metab. *1*, 1189–1201.
437 https://doi.org/10.1038/s42255-019-0148-2.

438 39. De Rosa, M.J., Veuthey, T., Florman, J., Grant, J., Blanco, M.G., Andersen, N.,
439 Donnelly, J., Rayes, D., and Alkema, M.J. (2019). The flight response impairs
440 cytoprotective mechanisms by activating the insulin pathway. Nature *573*, 135–138.
441 https://doi.org/10.1038/s41586-019-1524-5.

442 40. Hampton, R.F., Jimenez-Gonzalez, M., and Stanley, S.A. (2022). Unravelling
443 innervation of pancreatic islets. Diabetologia *65*, 1069–1084.
444 https://doi.org/10.1007/s00125-022-05691-9.

445 41. Ulrich-Lai, Y.M., and Herman, J.P. (2009). Neural regulation of endocrine and
446 autonomic stress responses. Nat. Rev. Neurosci. *10*, 397–409.
447 https://doi.org/10.1038/nrn2647.

448 42. Sun, C., Wang, X., Hui, Y., Fukui, H., Wang, B., and Miwa, H. (2021). The Potential

Role of REG Family Proteins in Inflammatory and Inflammation-Associated Diseases of the Gastrointestinal Tract. Int. J. Mol. Sci. *22*, 7196. https://doi.org/10.3390/ijms22137196.

43. Chen, W., Imasaka, M., Lee, M., Fukui, H., Nishiura, H., and Ohmuraya, M. (2023). Reg family proteins contribute to inflammation and pancreatic stellate cells activation in chronic pancreatitis. Sci. Rep. *13*, 12201. https://doi.org/10.1038/s41598-023-39178-3.

44. Yu, L., Wu, Q., Jiang, S., Liu, J., Liu, J., and Chen, G. (2025). Controversial Roles of Regenerating Family Proteins in Tissue Repair and Tumor Development. Biomedicines *13*, 24. https://doi.org/10.3390/biomedicines13010024.

45. Okamoto, H. (1999). The Reg gene family and Reg proteins: with special attention to the regeneration of pancreatic β-cells. J. Hep. Bil. Pancr. Surg. *6*, 254–262. https://doi.org/10.1007/s005340050115.

Methods

Ethical approval

All animal experiments conducted in this study were approved by the Institutional Animal Ethics Committee of the Shanghai Cancer Institute (A2024170-004), Ren Ji Hospital, School of Medicine, Shanghai Jiao Tong University. Experiments were performed strictly in accordance with institutional guidelines and ethical standards.

Animals

Male C57BL/6J mice (8-10 weeks old) were obtained from Vitalriver and maintained under specific pathogen-free conditions (temperature: 22 ± 2 °C; humidity: 55% ± 5%; 12-h light/dark cycle) at Shanghai Jiao Tong University, with ad libitum access to standard rodent chow and water. Body weight, food intake, and water consumption were recorded regularly. All animal procedures were approved by the Institutional Animal Care and Use Committee (IACUC) of Shanghai Jiao Tong University and followed the NIH Guide for the Care and Use of Laboratory Animals.

Whole-organ clearing and labeling

Tissue harvesting

Mice were deeply anesthetized via intraperitoneal (i.p.) injection of sodium pentobarbital (50 mg/kg, RWD, r510-22) and perfused transcardially with phosphate-buffered saline (PBS, Servicebio, G4202) followed by 4% paraformaldehyde (PFA, Servicebio, G1101). The pancreas was carefully dissected, rinsed in PBS, and placed

486 on a moist filter paper. To preserve the organ's spatial architecture, the pancreas was
487 gently spread out and pinned at the edges using fine needles (Extended Data Fig.1a).

488 ***3D immunolabeling***

489 The sample was treated with methanol solutions for 3 days at room temperature and
490 bleached with a 5% H_2O_2 solution overnight at 4°C. Then, the sample was treated with
491 0.2% Triton X-100 solution for 3 days at room temperature with shaking. Subsequently,
492 the sample was immersed in a 10% donkey serum blocking solution for 3 days at room
493 temperature, followed by incubation in the primary antibody solution (TH, 1:500, rabbit,
494 ab112, Abcam; Insulin, 1:500, rat, MAB1417, R&D Systems) for 6 days at room
495 temperature, and then in the secondary antibody solution (donkey anti-rabbit 561 nm,
496 1:500, A32794, Invitrogen; donkey anti-rat 488 nm, 1:500, A21208, Invitrogen; DAPI,
497 1:500, D1306, Invitrogen) for 6 days at room temperature. After immersion in the
498 antibody solutions, the sample was washed with 0.2% Tween-20 solution for 2 days at
499 room temperature[46]. Detailed antibody information is summarized in Table 1.

500 ***Clearing method***

501 The FDISCO (fluorescence imaging of solvent-cleared organs with superior
502 fluorescence-preserving capability) tissue clearing reagent kit (JA11012, Jarvisbio) was
503 used in this study[47]. The clearing procedure was performed strictly according to the
504 manufacturer's instructions. Briefly, labeled mouse pancreas samples were sequentially
505 incubated in reagents A, B, C, and D for 6 hours each, followed by reagent E for 12
506 hours, and finally incubated in reagent F until complete transparency was achieved. All
507 incubations were conducted at 6-8 °C with gentle shaking.

508 **3D fluorescence imaging and digital reconstruction of cleared tissues**

509 ***Light-sheet microscope***

510 The cleared samples were imaged using a light sheet microscope (LiToneXL, Light
511 Innovation Technology) equipped with a 4× objective lens (NA = 0.28, working
512 distance = 20 mm). Thin light sheets were illuminated from the four sides of samples,
513 and a merged image was saved. To acquire images, the cleared samples were manually
514 attached to the sample holder adapter. Subsequently, the samples were immersed in
515 imaging reagent within a 3D printing sample chamber and excited with light sheets of
516 different wavelengths.

517 ***Confocal microscope***

518 The cleared tissue samples were mounted on two cover glasses and imaged using an
519 inverted confocal fluorescence microscope (LSM880, Zeiss, Germany) equipped with
520 the Plan Apochromat 10×/0.45 objective (dry lens; working distance = 2.0 mm), Plan
521 Apochromat 20×/0.8 objective (dry lens; working distance = 0.55 mm), and Plan
522 Apochromat 40×/0.95 objective (water immersion lens; working distance = 0.20 mm).
523 The collected images were subsequently processed with Zen software (Zeiss, Germany)
524 and reconstructed into 3D images using Imaris software (Version 7.2.3, Bitplane,
525 Switzerland)[48].

526 ***Imaging data processing***

527 The resulting TIFF raw data images were stitched and converted using LitScan software
528 and subsequently analyzed with Imaris software[48].

529 ***Digital reconstruction and quantitative analysis of cleared nerve fibers***

530 The Filament module of Imaris software was used for 3D tracing of nerve fibers in
531 cleared tissues. Cone mode and AutoDepth mode were selected to accurately locate and
532 delineate the nerve fibers, and the segment diameters were adjusted according to the
533 actual diameters of nerve trunks and branches. Finally, filament length and branching
534 points were quantified using the statistics panel of the Filament module.
535
536 **Islet isolation and renal subcapsular transplantation**
537 Pancreatic islets were isolated from donor mice using collagenase P (Roche, CollP-RO)
538 digestion and density gradient centrifugation as previously described[49]. Approximately
539 500 islets were evenly divided into two parts and transplanted under the bilateral renal
540 capsule of STZ-induced diabetic recipient mice. For transplantation, mice were
541 anesthetized, and a small incision was made to expose the kidney. Islets were
542 transferred using a Hamilton syringe and gently injected under the renal capsule. The
543 incision was closed with surgical sutures, and mice were allowed to recover with
544 appropriate postoperative care.
545
546 **Establishment of diabetic mice models**
547 Two distinct protocols for streptozotocin (STZ)-induced diabetes were employed,
548 depending on the experimental purpose. Specifically, a multiple low-dose STZ protocol
549 was used to establish stable diabetes for subsequent islet transplantation experiments.
550 A single high-dose STZ injection was administered one day after sympathetic nerve
551 ablation using 6-hydroxydopamine (6-OHDA) to rapidly induce severe β-cell injury,

552 thus preventing potential confounding effects of residual functional islets on
553 sympathetic nerve regeneration.

554 ***Multiple low-dose STZ induction***

555 Diabetes was induced by daily i.p. injections of STZ (50 mg/kg) dissolved in 0.1 M
556 citrate buffer (pH 4.2-4.5), administered over five consecutive days[50].

557 ***Single high-dose STZ induction following 6-OHDA treatment***

558 Diabetes was induced by a single high-dose i.p. injection of STZ (150 mg/kg), also
559 dissolved in 0.1 M citrate buffer (pH 4.2-4.5)[51]. The injection was given following an
560 8-hour fasting period, specifically one day after pancreatic sympathetic nerve ablation
561 using 6-OHDA.

562 Blood glucose levels were monitored every other day using a glucometer (Accu-Chek,
563 Roche). Mice were defined as diabetic when blood glucose exceeded 16.7 mmol/L in
564 three consecutive measurements.

565

566 **Blood glucose measurement and IPGTT**

567 Random blood glucose levels were measured from tail vein blood using a glucometer.
568 IPGTT were performed after an 8-hour fasting. Mice received an i.p. injection of
569 glucose (2 g/kg), and blood glucose levels were measured at 0, 15, 30, 60, and 120 min
570 post-injection[52].

571

572 **Sympathetic nerve ablation**

573 10-week-old mice were randomly assigned into the vehicle group and the 6-OHDA

574 group. After anesthetizing the mice with isoflurane, the hair in the abdomen was
575 removed and the area was disinfected with povidone-iodine. Then, a small incision was
576 made along the midline of the abdomen skin to expose the pancreas. The pancreas was
577 pulled out gently and fully exposed with sterile tweezers. 6-OHDA (HY-B1081, MCE)
578 was administered by intrapancreatic injection (1 mg in 15 μL saline containing 0.1%
579 L-ascorbic acid [HY-B0166, MCE], 100 mg/kg). To pharmacologically ablate
580 sympathetic nerve in the whole pancreas, this 15-μL dose of 6-OHDA was evenly
581 administered from the pancreas head to the tail. Control mice received a 15-μL dose of
582 0.1% L-ascorbic acid injections.
583
584 **Regenerating protein family (Reg-family) protein administration**
585 Recipient mice were randomly divided into four experimental groups:
586 ***Local administration***
587 Recombinant Reg2 (rReg2) and recombinant Reg3β (rReg3β) proteins (500 nM final
588 concentration) were incorporated into a biocompatible hydrogel matrix (Corning,
589 Cat#354236) at a final concentration of 2 mg/mL. Isolated islets were gently mixed
590 with the Reg-loaded hydrogel. Controls received islets embedded in hydrogel without
591 Reg proteins.
592 ***Systemic administration***
593 Mice received purified islets embedded in a hydrogel matrix (2 mg/mL, Corning,
594 Cat#354236). For the systemic administration group, mice additionally received i.p.
595 injections of rReg2 and rReg3β protein mixture (150 mg/kg, dissolved in sterile ddH_2O

596 at 100 mg/mL) on days 1, 3, and 5 post-transplantation[53,54], starting on the
597 transplantation day. Controls received equal volumes of sterile ddH_2O on the same
598 schedule.
599 All animal procedures were performed under general anesthesia, following institutional
600 animal care and use guidelines.
601
602 **Lentiviral-mediated knockdown of *Reg2* and *Reg3b* expression in pancreatic islets**
603 ***shRNA design and vector construction***
604 Three independent shRNA sequences targeting mouse *Reg2* (NCBI Gene ID:
605 NM_009043.2) and *Reg3b* (NCBI Gene ID: NM_011036.1), along with a scrambled
606 control shRNA, were designed and synthesized **(Supplementary Table 2)**. Each
607 sequence was cloned into the lentiviral vector pSLenti-U6-shRNA-CMV-EGFP-F2A-
608 Puro-WPRE.
609 ***Validation of shRNA knockdown efficiency in isolated islets***
610 Freshly isolated mouse pancreatic islets (approximately 100 islet equivalents, IEQ)
611 were pre-cultured overnight in RPMI-1640 medium supplemented with 10% fetal
612 bovine serum (FBS). Equal volumes of lentiviral preparations containing three distinct
613 shRNAs targeting either *Reg2* or *Reg3b* were pre-mixed at a 1:1:1 ratio, ensuring equal
614 multiplicity of infection (MOI) distribution for each shRNA construct. The pooled
615 lentiviral mixtures were added to the pre-cultured islet at a total MOI of 10-20 in the
616 presence of polybrene (10 μg/mL). After incubation at 37°C for 8 h, the virus-
617 containing medium was replaced with fresh culture medium. Gene knockdown

618 efficiency was confirmed by RT-qPCR analysis prior to islet transplantation (see
619 Extended Data Fig.7).

620 ***Lentiviral-mediated shRNA delivery during islet transplantation***

621 To achieve efficient *Reg2* and *Reg3b* knockdown during islet transplantation, freshly
622 isolated pancreatic islets were mixed with lentiviral preparations (containing the same
623 shRNA mixture described above) and rapidly encapsulated in a hydrogel matrix. The
624 islet-lentivirus-hydrogel mixture was then incubated for approximately 30 min at 37°C
625 to allow complete gelation, and subsequently transplanted beneath the renal capsule of
626 anesthetized recipient mice.

627

628 **Real-time quantitative PCR （RT-qPCR）**

629 Total RNA was extracted from tissues or cells using TRIzol reagent (Invitrogen). cDNA
630 was synthesized using the PrimeScript RT reagent Kit (Takara). RT-qPCR was
631 performed with SYBR Green PCR Master Mix (Applied Biosystems) on a QuantStudio
632 6 Flex Real-Time PCR System (Applied Biosystems). Gene expression levels were
633 normalized to β-actin and calculated using the $2^{\wedge-\Delta\Delta Ct}$ method. Primer sequences are
634 listed in Supplementary Table 3.

635

636 **Transcriptome sequencing of laser-captured pancreatic islets**

637 ***Sample preparing***

638 Formalin-fixed, paraffin-embedded (FFPE) pancreatic tissue was sectioned at 7 μm
639 thickness. Slides were first deparaffinized in xylene for 5 min, rehydrated sequentially

640 through graded ethanol solutions (100%, 95%, 70%, and 50%; 2 min each), and rinsed
641 briefly in distilled water. Sections were then rapidly stained with hematoxylin and eosin
642 (H&E) using an optimized protocol designed to preserve RNA integrity. Following
643 staining, slides were dehydrated in ascending ethanol concentrations, cleared with
644 xylene, and allowed to air-dry completely under RNase-free conditions before further
645 processing.

646 ***Laser-capture microdissection (LCM) and libraries preparation***

647 LCM was performed using a PALM MicroBeam system (Zeiss MicroImaging, Munich,
648 Germany). Islet regions were identified based on morphological criteria under
649 microscopic observation. Approximately 300 islets per sample were precisely isolated
650 via laser microdissection and collected into 200 μL adhesive-capped tubes (Carl Zeiss,
651 cat.no. 415190-9191-000, Jena, Germany). Immediately following collection, 10 μL of
652 LCM lysis mix buffer was added, and tubes were sealed tightly with Parafilm.
653 Transcriptome libraries were generated following the Smart-3SEQ protocol. Briefly,
654 cell lysis and RNA fragmentation were performed at 60°C for 60 min, followed by the
655 addition of 10 μL LCM TS-RT mix for reverse transcription. Amplification of the
656 resulting cDNA and subsequent cleanup were performed according to the published
657 protocol. The final library concentration was measured using a Qubit 3.0 fluorometer
658 (Thermo Fisher Scientific, MA, USA)[55,56].

659 ***Next-generation sequencing***

660 The cDNA libraries were profiled for size distribution on an Agilent 2100 with High
661 Sensitivity D1000 reagent kit (Agilent, Santa Clara, USA) and then stored at -20°C

662 until sequencing. The libraries were sequenced using the Illumina high-throughput
663 sequencing platform NovaSeq 6000 system (Illumina, San Diego, USA) with 2x 150
664 bp pair-end mode.

665 ***Data analysis***

666 The FASTQ data were analyzed according to the Smart-3SEQ protocol. Briefly, base
667 calls from the NovaSeq were demultiplexed and converted to FASTQ format and
668 adapter trimming were performed. The first 5nt of each read were removed from its
669 sequence and appended to the read name as its UMI; the following 3nt were assumed
670 to derive from the G-overhand of the template-switch oligonucleotide and were
671 discarded. Reads were aligned by STAR to the mouse reference genome mm10. PCR
672 duplicate reads that start at the same genome position with the same UMI sequence
673 were detected and discarded. Then the transcript abundance was quantified. Differential
674 gene expression was analyzed with DESeq2. The regularized log transformation was
675 used to normalize read counts. PCA was performed on the normalized data with the
676 prcomp function.

677

678 **Bulk RNA-seq of isolated pancreatic islets**

679 Pancreatic islets were isolated from 0.1% L-ascorbic acid or 6-OHDA treated mice
680 using collagenase P (Roche, CollP-RO) digestion and density gradient centrifugation
681 as previously described. Total RNA was extracted from islet samples with the Universal
682 RNA Extraction CZ Kit (RNC643, ONREW) according to the manufacturer's
683 instructions. RNA quantity was analysed using Qubit 4.0 (Invitrogen) and quality

examined by electrophoresis on a denaturing agarose gel. RNA libraries were prepared using the VVAHTS® Universal V8 RNA-seq Library Prep Kit for Illumina (NR605-0, Vazyme), followed sequencing using the Illumina NovaSeq 6000 platform with the 150 paired-end sequencing strategy. Enrichment of mRNA, library construction, sequencing and data analysis were performed by Shanghai Xu Ran Biotechnology Co., Ltd. The raw data was handled by Skewer v0.2.2 (https://sourceforge.net/projects/skewer/files/?source=navbar) and data quality was checked by FastQC v0.11.2 (http://www.bioinformatics.babraham.ac.uk/projects/fastqc/). The read length was 2×150 bp. Clean reads were aligned to the mouse genome GRCm39 (mm10) from ensembl using STAR (https://github.com/alexdobin/STAR), with one mismatch allowed. StringTie (v1.3.1c) was used to generate gene expression data and differential gene expression was analysed by DESeq2 (v1.16.1) (https://bioconductor.org/packages/release/bioc/html/DESeq2.html). The thresholds for determining DEGs are $P < 0.05$ and absolute fold change ≥ 2. Then DEGs were chosen for function and signaling pathway enrichment analysis using TopGO (https://www.bioconductor.org/packages/release/bioc/html/topGO.html) and KEGG database (https://www.genome.jp/kegg/pathway.html). The significantly enriched pathways were determined when $P < 0.05$.

706 ***Data availability***

707 The raw sequencing data from the laser capture microdissected samples and the isolated
708 islet samples have been deposited in the NCBI SRA under accession number
709 PRJNA1241420 and PRJNA1243594 respectively. All other data in this article are
710 available from the corresponding author on reasonable request.

711

712 **References: Methods**

713 46. Nicolas Renier, Adams, E.L., Kirst, C., Wu, Z., Azevedo, R., Kohl, J., Autry, A.E.,
714 Kadiri, L., Venkataraju, K.U., Zhou, Y., et al. (2016). Mapping of Brain Activity by
715 Automated Volume Analysis of Immediate Early Genes. Cell *165*, 1789–1802.
716 https://doi.org/10.1016/j.cell.2016.05.007.

717 47. Qi, Y., Yu, T., Xu, J., Wan, P., Ma, Y., Zhu, J., Li, Y., Gong, H., Luo, Q., and Zhu,
718 D. (2019). FDISCO: Advanced solvent-based clearing method for imaging whole
719 organs. Sci. Adv. *5*, eaau8355. https://doi.org/10.1126/sciadv.aau8355.

720 48. Zhu, J., Liu, X., Liu, Z., Deng, Y., Xu, J., Liu, K., Zhang, R., Meng, X., Fei, P., Yu,
721 T., et al. (2024). SOLID: minimizing tissue distortion for brain-wide profiling of diverse
722 architectures. Nat. Commun. *15*, 8303. https://doi.org/10.1038/s41467-024-52560-7.

723 49. Wang, K., Wang, X., Han, C.-S., Chen, L.-Y., and Luo, Y. (2017). Scaffold-
724 supported Transplantation of Islets in the Epididymal Fat Pad of Diabetic Mice. J. Vis.
725 Exp., 54995. https://doi.org/10.3791/54995.

726 50. Chaudhry, Z.Z., Morris, D.L., Moss, D.R., Sims, E.K., Chiong, Y., Kono, T., and

Evans-Molina, C. (2013). Streptozotocin is equally diabetogenic whether administered to fed or fasted mice. Lab. Anim. *47*, 257–265. https://doi.org/10.1177/0023677213489548.

51. Chen, H., Liu, J., Shi, G.-P., and Zhang, X. (2023). Protocol for in vivo and ex vivo assessment of hyperglycemia and islet function in diabetic mice. Star. Protoc. *4*, 102133. https://doi.org/10.1016/j.xpro.2023.102133.

52. Basco, D., Zhang, Q., Salehi, A., Tarasov, A., Dolci, W., Herrera, P., Spiliotis, I., Berney, X., Tarussio, D., Rorsman, P., et al. (2018). α-cell glucokinase suppresses glucose-regulated glucagon secretion. Nat. Commun. *9*, 546. https://doi.org/10.1038/s41467-018-03034-0.

53. Luo, C., Yu, L.-T., Yang, M.-Q., Li, X., Zhang, Z.-Y., Alfred, M.O., Liu, J.-L., and Wang, M. (2016). Recombinant Reg3β protein protects against streptozotocin-induced β-cell damage and diabetes. Sci. Rep. *6*, 35640. https://doi.org/10.1038/srep35640.

54. Yu, L., Li, X., Zhang, Z., Du, P., Liu, J.-L., Li, Y., Yin, T., Yu, W., Sun, H., Wang, M., et al. (2019). Dimorphic autoantigenic and protective effects of Reg2 peptide in the treatment of diabetic β-cell loss. Diabetes. Obes. Metab. *21*, 1209–1222. https://doi.org/10.1111/dom.13644.

55. Zhang, X., Hu, C., Huang, C., Wei, Y., Li, X., Hu, M., Li, H., Wu, J., Czajkowsky, D.M., Guo, Y., et al. (2022). Robust Acquisition of Spatial Transcriptional Programs in Tissues With Immunofluorescence-Guided Laser Capture Microdissection. Front. Cell. Dev. Biol. *10*, 853188. https://doi.org/10.3389/fcell.2022.853188.

56. Wu, Z., Wu, X., Xu, Z., Liu, Y., Zhu, Z., Li, X., Czajkowsky, D.M., Sun, F., Guo, Y., and Shao, Z. (2025). In situ transcriptomic analysis of spermatocytes in non-obstructive azoospermia reveals senescence-like states in arrested spermatocytes. GENES. DIS. *12*, 101205. https://doi.org/10.1016/j.gendis.2024.101205.

Acknowledgements

This study was supported by the National Natural Science Foundation of China (92168111, 82230087, 82350123, 82203228), the Shanghai Municipal Education Commission-Gaofeng Clinical Medicine Grant Support (20181708), Innovative research team of high-level local universities in Shanghai (SHSMU-ZDCX20210802), Shanghai Pilot Program for Basic Research - Shanghai Jiao Tong University (21TQ1400225), 111 project (no. B21024), Shenyang Science and Technology Plan in 2022 (22-101-0-22).

Author contributions

Z.-G.Z. and D.-X.L. conceived the project and designed experiments. J.-M.L., J.-J.W., Y.-Z.Q., and D.-X.L. performed experiments and analyzed the data. D.-X.L. and J.-M.L. wrote the manuscript. J.-J.W. and H.-L. performed bioinformatics analyses. D.A., T.Y., Y.-X.H., W.-T.S., X.-Y.M., and M.M. assisted with experiments. L.Z., X.-M.Y., Y.Q., Y.-L.Z., and Y.-Q.Y. provided technical support. S.-H.J., J.L., L.-P.H., X.-L.Z., and Q.L. provided critical insights and revised the manuscript. All authors reviewed and approved the final manuscript.

770 **Competing interests**

771 The authors declare no competing interests.

772

773 **Figure legends**

774 **Figure 1. Pancreatic islets form a highly organized spatial arrangement along**

775 **sympathetic nerves.**

776 **a**, Whole-pancreas 3D imaging of an unfolded and cleared pancreas from an 8-week-

777 old male mouse (C57BL/6J) reveals a highly organized sympathetic neural network

778 (TH, magenta). Pancreatic islets (insulin, green) are precisely positioned along these

779 sympathetic nerve branches. Nuclei are stained with DAPI (blue). Scale bars: 2500 μm.

780 See Supplementary Video 1.

781 **b-d**, Magnified views of representative areas from (a).

782 **e,** High-resolution imaging of a pancreatic islet and sympathetic nerve fibers. Scale bars:

783 50 μm.

784 **f, g,** 3D reconstructions of the two individual islets shown in (e). Scale bars: 20 μm.

785

786 **Figure 2. Pancreatic islets actively recruit sympathetic nerves independent of the**

787 **pancreatic environment.**

788 **a,** Schematic illustration of the experimental strategy for renal subcapsular

789 transplantation of approximately 500 isolated pancreatic islets into STZ-induced

790 diabetic mice, to evaluate sympathetic nerve recruitment by islets transplanted outside

791 their native pancreatic environment.

792 **b,** Representative whole-kidney clearing images (left) showing sympathetic innervation
793 (TH, magenta), transplanted islets (insulin, green) at day 120 post-transplantation.
794 Corresponding 3D reconstructions (right) illustrate pre-existing sympathetic nerves
795 within the kidney (magenta), islet-recruited sympathetic nerves (yellow), transplanted
796 islets (green), and the adrenal gland (blue), viewed horizontally (0°) and from a tilted
797 angle (45°). White arrowheads indicate sympathetic fibers clearly directed toward the
798 transplanted islets. Sham-operated mice served as controls and exhibited no significant
799 sympathetic nerve recruitment. Scale bars: 1000 μm. See Supplementary Video 4 for
800 dynamic visualization.
801 **c, d,** Quantitative analyses of sympathetic nerve growth recruited by transplanted islets,
802 including total nerve length (c) and branch number (d), assessed at multiple time points
803 (days 10, 20, 30, 40, 50, and 120) post-transplantation. Corresponding whole-tissue
804 clearing and 3D reconstructions for each time point are presented in Supplementary
805 Fig.3 and Supplementary Video 4-9.
806
807 **Figure 3. Islets maintain pancreatic sympathetic innervation and facilitate**
808 **regeneration following denervation.**
809 **a,** Representative whole-pancreas 3D imaging showing sympathetic nerves (TH,
810 magenta), pancreatic islets (insulin, green), and nuclei (DAPI, blue) in control mice
811 (left) and mice subjected to chronic islet injury induced by STZ for 140 days (right).
812 Scale bars: 2500 μm. See Supplementary Videos 10 and 11.

813 **b,** Time-course imaging of sympathetic nerve regeneration following selective
814 sympathetic nerve ablation using intrapancreatic 6-hydroxydopamine (6-OHDA)
815 injection. Upper: significant sympathetic (TH, magenta) regeneration and restoration
816 of structured associations with islets (insulin, green) at days 47, 56, and 65 post-
817 denervation. Lower: impaired sympathetic regeneration at corresponding time points in
818 mice subjected to severe islet injury induced by STZ administration one day post-
819 denervation. Scale bars: 2500 μm. See Supplementary Videos 15-20.
820
821 **Figure 4. Reg-family proteins, particularly Reg2 and Reg3β, are prominently**
822 **upregulated in pancreatic islets following sympathetic denervation.**
823 **a,** Schematic illustration of laser-capture microdissection (LCM) procedure for precise
824 isolation of pancreatic islets from pancreas tissue on day 7 post-sympathetic
825 denervation for mRNA sequencing.
826 **b,** mRNA sequencing analysis of LCM-isolated islets revealed different expression
827 genes (DEGs) post-denervation (n = 3 per group).
828 **c,** Experimental workflow illustrating conventional isolation of pancreatic islets at
829 multiple time points (days 3, 7, 14, and 21) post-sympathetic denervation for RNA
830 sequencing analysis.
831 **d,** mRNA sequencing-based temporal expression profiles of Reg-family genes in
832 conventionally isolated islets post-denervation (n = 3 per group per time point).
833 **e,** Real-time quantitative PCR (RT-qPCR) validation of *Reg2 and Reg3b* expression at
834 indicated time points using samples from (d) (n = 3 per group per time point). Data

835 presented as mean ± SEM, analyzed by two-tailed Student's t-test. *$P < 0.05$, **$P <$
836 0.01, ***$P < 0.001$.
837
838 **Figure 5. Exogenous rReg2 and rReg3β enhance sympathetic nerve regeneration**
839 **and improve functional outcomes in transplanted islets.**
840 **a,** Representative whole-kidney clearing images (left) showing sympathetic nerves (TH,
841 magenta), transplanted islets (insulin, green) at day 50 post-transplantation.
842 Corresponding 3D reconstructions (right) illustrate pre-existing renal sympathetic
843 nerves (magenta), islet-recruited sympathetic nerves (yellow), transplanted islets
844 (green), and the adrenal gland (blue). White arrowheads indicate sympathetic nerves
845 extending toward islets. Recombinant regenerating protein 2 (rReg2) and recombinant
846 regenerating protein 3 beta (rReg3β) proteins were incorporated into hydrogel during
847 gelation, thereby achieving localized drug delivery to islet grafts. Scale bar, 1000 μm.
848 See Supplementary Video 24.
849 **b,** Quantification of sympathetic nerve fibers extending toward transplanted islets
850 following localized hydrogel delivery of rReg2 and rReg3β proteins, as illustrated in (a)
851 (n = 4 per group).
852 **c,** Representative whole-kidney clearing images (left) at day 35 post-transplantation
853 showing sympathetic nerves (TH, magenta), transplanted islets (insulin, green).
854 Corresponding 3D reconstructions (right) illustrate pre-existing renal sympathetic
855 nerves (magenta), islet-recruited sympathetic nerves (yellow), transplanted islets
856 (green), and the adrenal gland (blue). White arrowheads indicate sympathetic nerves

857 extending toward islets. rReg2 and rReg3β proteins were systemically administered via
858 intraperitoneal (i.p.) injections on days 1, 3, and 5 post-transplantation. Scale bar, 1000
859 μm. See Supplementary Video 25.
860 **d,** Quantification of sympathetic nerve fibers extending toward transplanted islets
861 following i.p. injection of rReg2 and rReg3β proteins, as illustrated in (c) (n = 3 per
862 group).
863 **e,** Representative whole-kidney clearing images (left) at day 60 post-transplantation
864 showing sympathetic nerves (TH, magenta) and transplanted islets (insulin, green).
865 Corresponding 3D reconstructions (right) illustrate pre-existing renal sympathetic
866 nerves (magenta), islet-recruited sympathetic nerves (yellow), transplanted islets
867 (green), and adrenal gland (blue), following lentiviral-mediated knockdown of *Reg2*
868 and *Reg3b*. White arrowheads indicate sympathetic nerves extending toward islets.
869 Knockdown efficiency was verified by RT-qPCR (Supplementary Fig.5d); shRNA
870 sequences provided in Supplementary Table 1. Scale bar, 1000 μm. See Supplementary
871 Video 26.
872 **f,** Quantification of sympathetic nerve fibers extending toward transplanted islets
873 following lentiviral-mediated knockdown of *Reg2* and *Reg3b*, as illustrated in (e) (n =
874 3 per group).
875 **g, h,** IPGTT at days 30 (g) and 50 (h) post-transplantation. Notably, the enhancement
876 in islet graft function was more pronounced at day 50 than at day 30 (n = 3-4 per group
877 per time point). Corresponding whole-kidney clearing images are shown in
878 Supplementary Video 27.

879 Data are shown as mean ± SEM, analyzed by two-tailed Student's t-test. *$P < 0.05$, **P

880 < 0.01, ***$P < 0.001$.

881

882

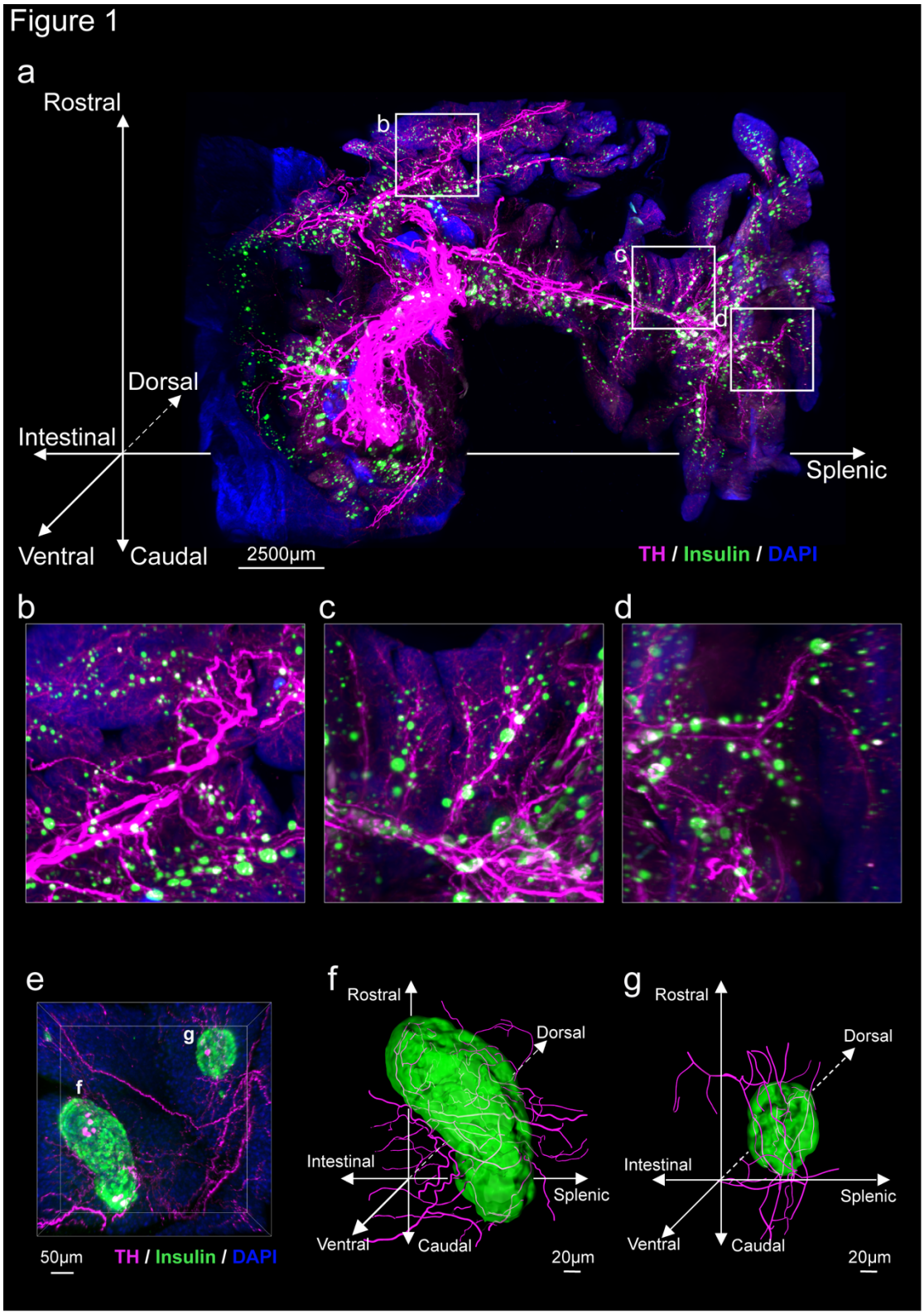
Figure 1
a
Rostral
Dorsal
Intestinal
Ventral
Caudal
Splenic
b
c
d
2500µm
TH / Insulin / DAPI
b
c
d
e
f
g
50µm
TH / Insulin / DAPI
f
Rostral
Dorsal
Intestinal
Splenic
Ventral
Caudal
20µm
g
Rostral
Dorsal
Intestinal
Splenic
Ventral
Caudal
20µm

883

Figure 2

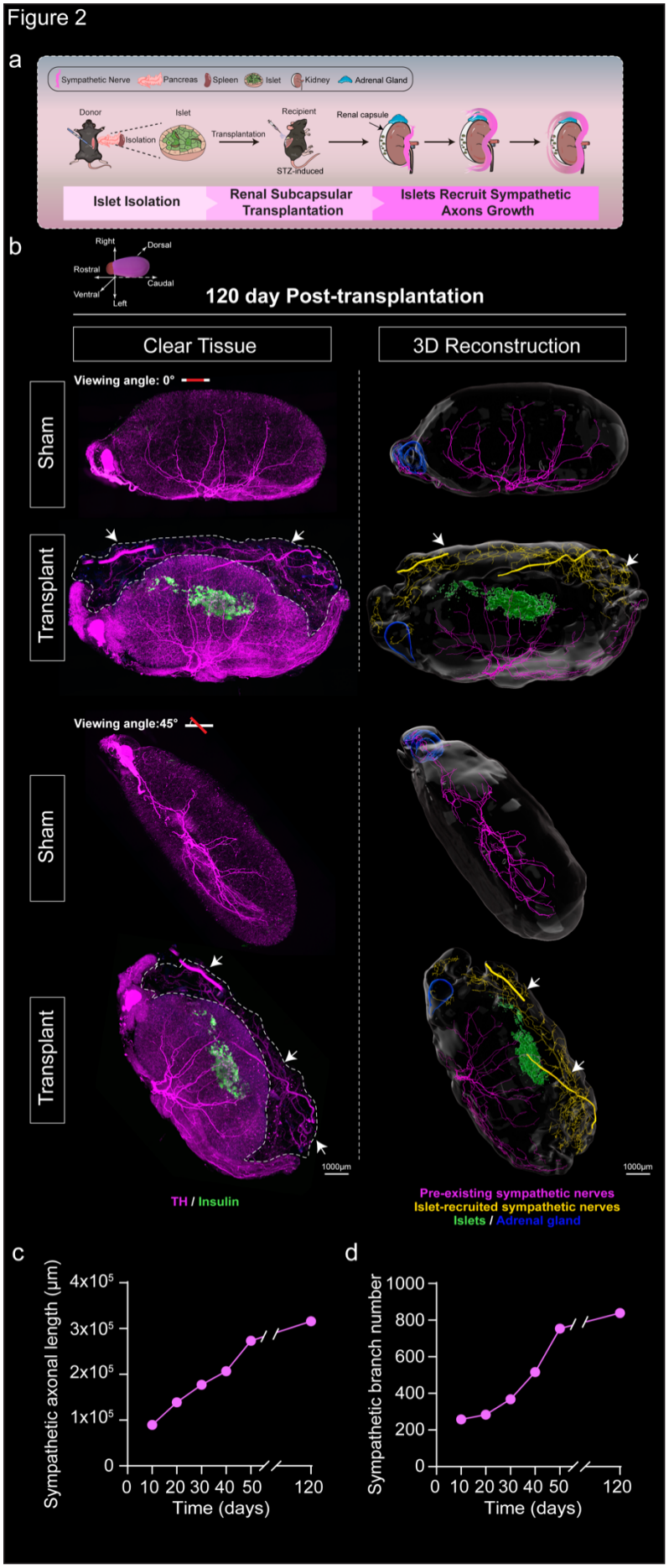
a
Sympathetic Nerve
Pancreas
Spleen
Islet
Kidney
Adrenal Gland
Donor
Islet
Isolation
Transplantation
Recipient
STZ-induced
Renal capsule
Islet Isolation
Renal Subcapsular Transplantation
Islets Recruit Sympathetic Axons Growth
b
Right
Dorsal
Rostral
Caudal
Ventral
Left
120 day Post-transplantation
Clear Tissue
3D Reconstruction
Viewing angle: 0°
Sham
Transplant
Viewing angle:45°
Sham
Transplant
1000µm
1000µm
TH / Insulin
Pre-existing sympathetic nerves
Islet-recruited sympathetic nerves
Islets / Adrenal gland
c
Sympathetic axonal length (µm)
4x10^5
3x10^5
2x10^5
1x10^5
0
0 10 20 30 40 50 120
Time (days)
d
Sympathetic branch number
1000
800
600
400
200
0
0 10 20 30 40 50 120
Time (days)

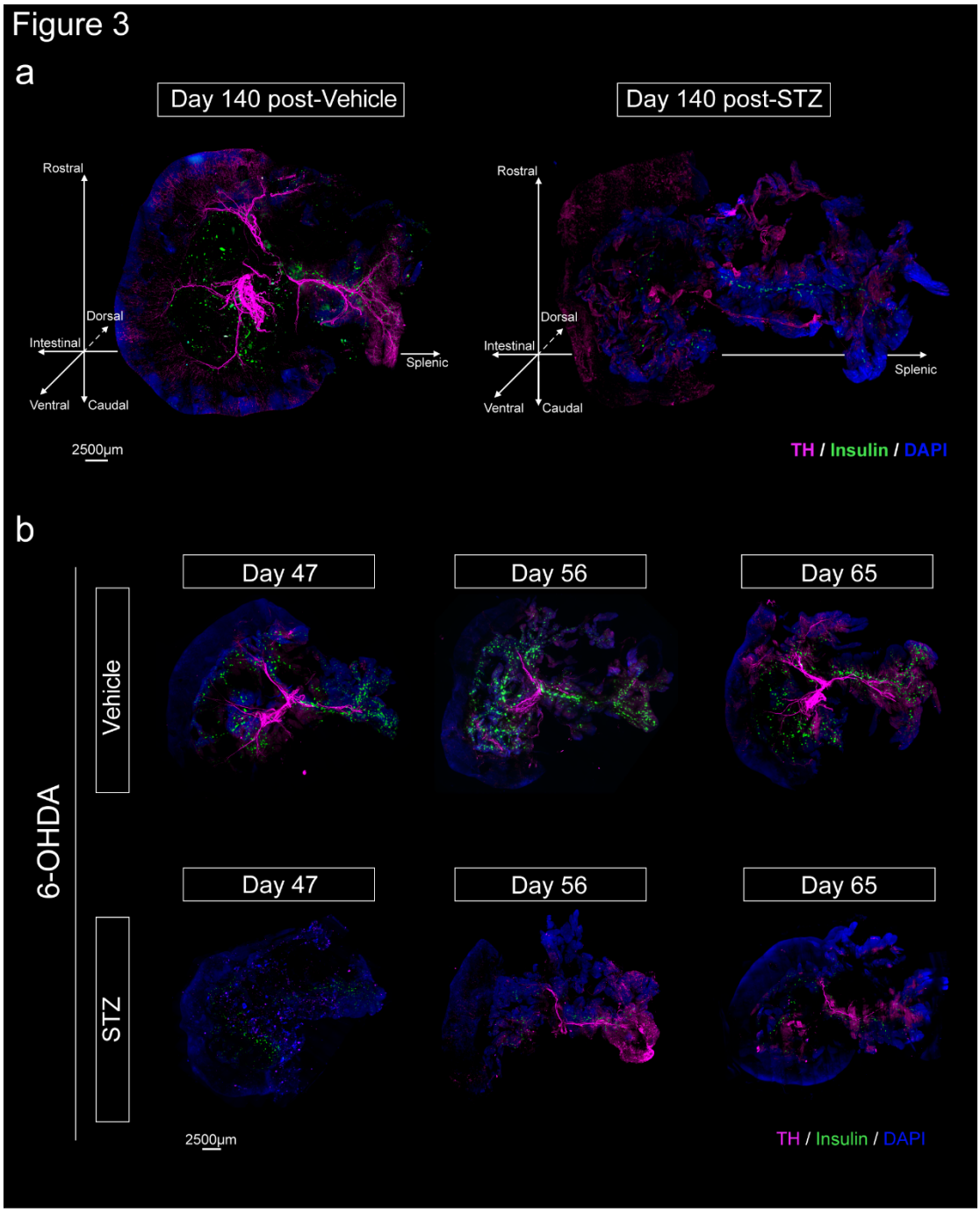
Figure 3
a
Day 140 post-Vehicle
Day 140 post-STZ
Rostral
Dorsal
Intestinal
Ventral
Caudal
Splenic
2500µm
TH / Insulin / DAPI
b
6-OHDA
Vehicle
STZ
Day 47
Day 56
Day 65
2500µm
TH / Insulin / DAPI

885

Figure 4

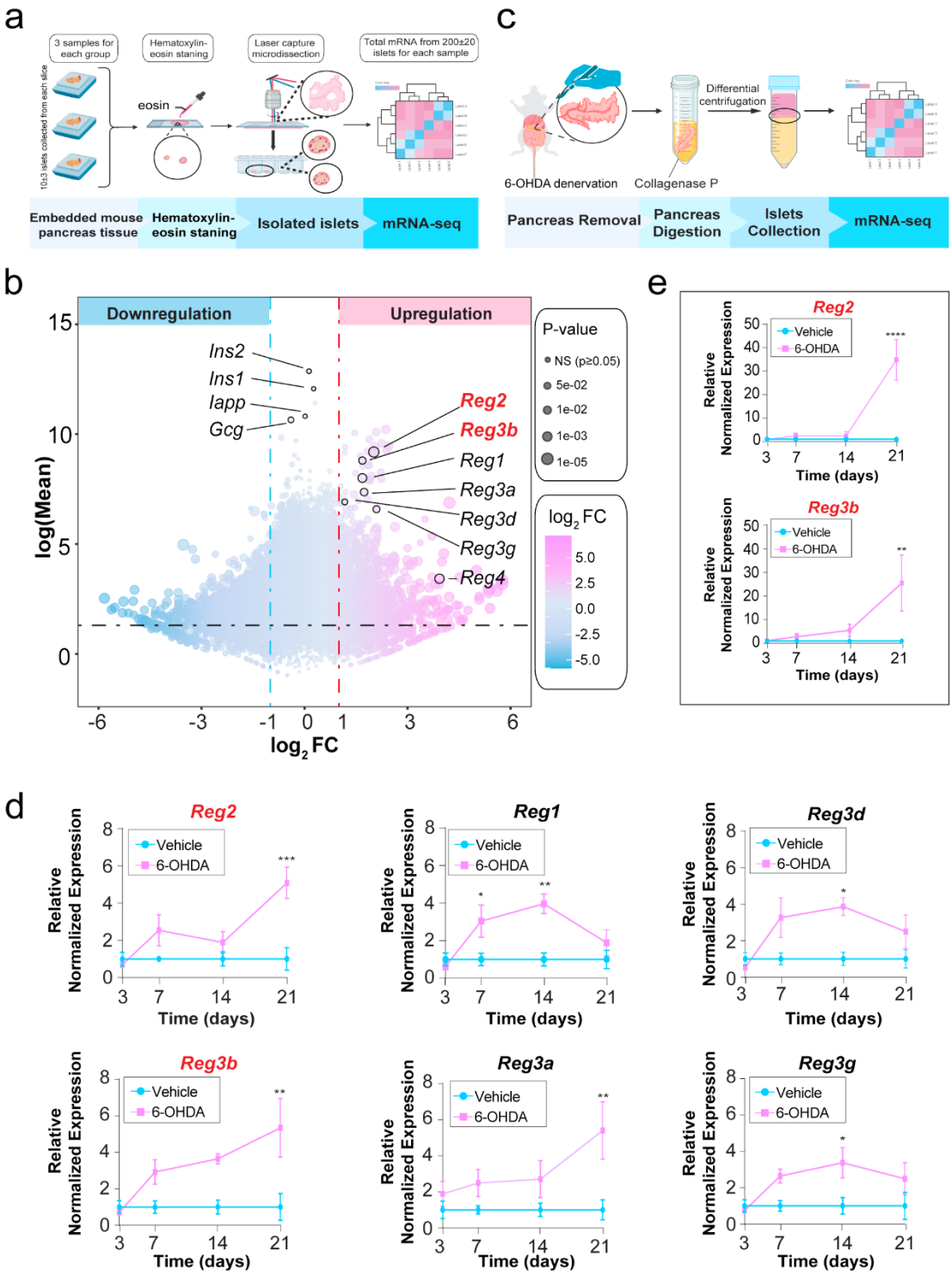
a
3 samples for each group
Hematoxylin-eosin staning
Laser capture microdissection
Total mRNA from 200±20 islets for each sample
10±3 islets collected from each slice
eosin
Embedded mouse pancreas tissue
Hematoxylin-eosin staning
Isolated islets
mRNA-seq
c
Differential centrifugation
6-OHDA denervation
Collagenase P
Pancreas Removal
Pancreas Digestion
Islets Collection
mRNA-seq
b
Downregulation
Upregulation
Ins2
Ins1
Iapp
Gcg
Reg2
Reg3b
Reg1
Reg3a
Reg3d
Reg3g
Reg4
P-value
NS (p≥0.05)
5e-02
1e-02
1e-03
1e-05
log2 FC
5.0
2.5
0.0
-2.5
-5.0
log(Mean)
log2 FC
e
Reg2
Reg3b
Vehicle
6-OHDA
Relative Normalized Expression
Time (days)
d
Reg2
Reg1
Reg3d
Reg3b
Reg3a
Reg3g
Vehicle
6-OHDA
Relative Normalized Expression
Time (days)

886

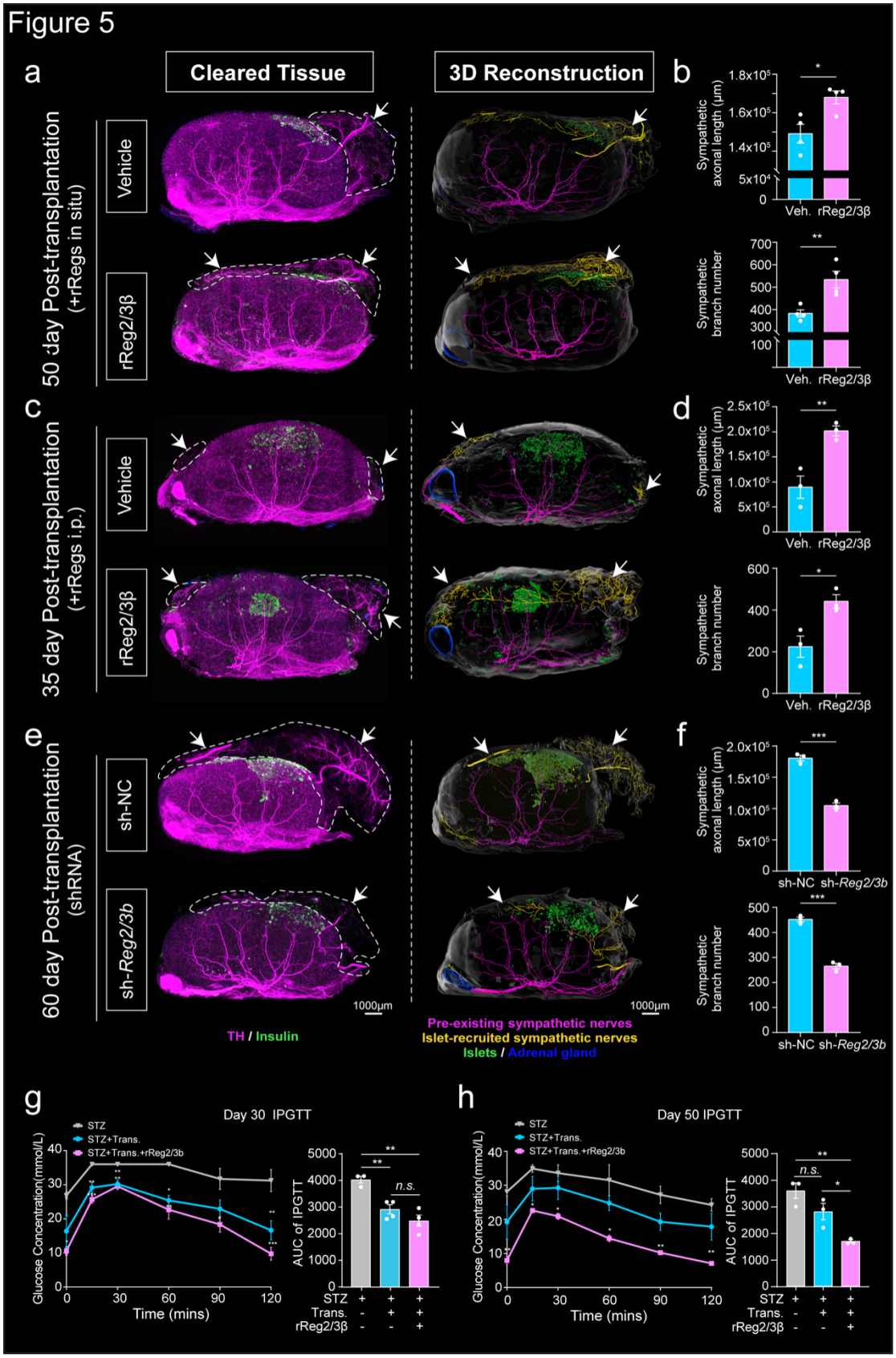
Figure 5
a
Cleared Tissue
3D Reconstruction
b
50 day Post-transplantation
(+rRegs in situ)
Vehicle
rReg2/3β
Sympathetic axonal length (μm)
Sympathetic branch number
Veh.
rReg2/3β
c
d
35 day Post-transplantation
(+rRegs i.p.)
e
f
60 day Post-transplantation
(shRNA)
sh-NC
sh-Reg2/3b
1000μm
TH / Insulin
Pre-existing sympathetic nerves
Islet-recruited sympathetic nerves
Islets / Adrenal gland
g
Day 30 IPGTT
STZ
STZ+Trans.
STZ+Trans.+rReg2/3b
Glucose Concentration(mmol/L)
Time (mins)
AUC of IPGTT
n.s.
Trans.
h
Day 50 IPGTT

887